Available online at www.sciencedirect.com
SCIENCE DIRECT
Journal of Power Sources 157 (2006) 85–97
JOURNAL OF POWER SOURCES
www.elsevier.com/locate/jpowsour

Effect of flow orientation on thermal-electrochemical transports in a PEM fuel cell

J.J. Hwang [a,*], C.H. Chao [b], W.Y. Ho [a], C.L. Chang [a], D.Y. Wang [a]

[a] *Research Center for Advanced Science and Technology, Mingdao University, 369 Wenhua Rd., Peetou, Changhua 52345, Taiwan*
[b] *Department of Electrical Engineering, Ta-Hua Institute of Technology, Hsinchu County 307, Taiwan*

Received 5 June 2005; received in revised form 15 July 2005; accepted 18 July 2005
Available online 13 September 2005

Abstract

A non-isothermal model of a proton exchange membrane (PEM) fuel cell in contact with interdigitated gas distributors has been performed. The model accounts for the major transports of convective and diffusive heat and mass transfer, electrode kinetics, and potential fields. The effects of flow orientation and total overpotential across a five-layer membrane-electrode assembly on the thermal behaviors in a PEM fuel cell are examined. A unique feature of the model is the implementation of a thermal-electrochemical algorithm to predict the fluid-phase temperature as well as the solid-matrix temperature in a PEM fuel cell. The simulation results reveal both the solid-matrix temperature and the fluid-phase temperature are increased with increasing total overpotential. Moreover, the fluid-phase and solid-matrix temperature distributions are significantly affected by the flow orientation in the PEM fuel cell. Replacing the parallel-flow geometry by the counter-flow geometry has an advantage of reducing the local maximum temperature inside the fuel cell. Thermal effects on the active material degradation and hence fuel cell durability will be incorporated in the future work.

Keywords: PEM fuel cell; Porous; Counter flow

1. Introduction

The irreversibility of electrochemical reactions is the majority of heat source in a proton exchange membrane (PEM) fuel cell, which raises the fluid temperature as well as the solid-matrix temperature during operation. The local temperature distribution inside a fuel cell has a strong impact on the fuel cell performance since it affects the water–vapor distribution by means of condensation. Insufficient cooling may result in local hot spots and thus dehydrate, shrink or even rupture the membrane. In addition, the kinetics of electrochemical reactions directly depends on temperature. Therefore, as far as the reliability and durability are concerned, an efficient thermal management of a PEM fuel cell becomes crucial. It includes not only the removal of the generated heat from inside the fuel cell to the outside but also the spatial uniformity of temperature distribution that avoids local hot spots.

In the past decade, numerous research efforts have been devoted to develop realistic simulation models. Notable early works include Bernardi and Verbrugge [1,2] and Springer and his co-workers [3,4]. These models are one-dimensional and only account for diffusive mass transport and electrochemical kinetics. Later on, several two-dimensional models were developed by Nguyen and White [5], Fuller and Newman [6], and Gurau et al. [7]. Most of these assume some concentration profile of reactant species along the channel except for [7], which accounts directly for convective mass transport. Recently, Shimpalee and Dutta [8] described a steady state, isothermal, three-dimensional, and single phase PEM fuel cell model. It used a commercial code to solve the complete Navier–Stokes equations. Zhou and Liu [9], Um and Wang [10], and Hwang et al. [11] described a 3-D model for PEM fuel cell. Their results agree well with their own experimental observations. It is interested to note

* Corresponding author. Tel.: +886 422540025; fax: +886 422518272.
E-mail address: azaijj@mdu.edu.tw (J.J. Hwang).

0378-7753/$ – see front matter © 2005 Elsevier B.V. All rights reserved.
doi:10.1016/j.jpowsour.2005.07.060

Nomenclature

c_i	mole concentration of the species i (mol m^{-3}), $c_i = \left[\frac{\omega_i/M_i}{\sum_j^N \omega_j/M_j}\right]\frac{P}{RT}$
D_i	diffusivity of species i (m^2 s^{-1})
F	Faraday's constant (96 487 C mol^{-1})
hv	interfacial heat transfer coefficient (volumetric) (W m^3 K^{-1})
i	current density (A m^{-2})
j	transfer current density (A m^{-3})
k_c	thermal conductivity of the solid phase in the catalyst layer (W K^{-1} m^{-1})
k_f	thermal conductivity of the fluid phase (W K^{-1} m^{-1})
k_s	thermal conductivity of the solid phase (W K^{-1} m^{-1})
M	molecular weight (kg mol^{-1})
p	pressure (Pa)
$p_{i,m}$	possibility of the electrolyte in the connection of the catalyst layer
$p_{i,s}$	possibility of the catalyst in the connection of the catalyst layer
R	universal gas constant (W mol^{-1} K^{-1})
S	source terms in the governing equations
T	temperature (K)
u	velocity vectors (m s^{-1})
x, y	coordinate system, Fig. 1 (m)

Greek symbols

α	symmetric factor
ε	porosity (gas diffusion layer)
ε_c	porosity of the catalyst layer
η_{tot}	total overpotential across the MEA (V)
κ	permeability (m^2)
μ	viscosity (m s^{-2})
ρ	density (kg m^3)
σ_m	ionic conductivity of the membrane phase (Ω^{-1} m^{-1})
σ_s	electric conductivity of the catalyst phase (Ω^{-1} m^{-1})
τ	tortuosity
ϕ_m	potential of the ionic conductor (electrolyte phase) (V)
ϕ_s	potential of the electric conductor (catalyst phase) (V)
υ_m	volume fraction of the ionic conductor (electrolyte phase) in the catalyst layer
υ_s	volume fraction of the electric conductor (catalyst phase) in the catalyst layer
ω	mass fraction

Subscript

a	anode
c	catalyst or cathode
eff	effective
e	energy
f	fluid
HOR	hydrogen oxidation reaction
i	species
j	electricity
m	membrane phase, momentum
o	exchange current density
ORR	oxygen reduction reaction
ref	reference
s	solid, catalyst phase
T	transfer current
tot	total

that all above predicted results are based on the isothermal model.

The present study is aimed to develop a non-isothermal model to examine the thermal-electrochemical characteristics inside a PEM fuel cell. A set of conservation equations of mass, momentum, energy, species and charge is developed and solved numerically with proper account of electrochemical kinetics and fluid dynamics. The Brinkman extension to Darcy flow describes the fluid flow characteristics in the porous electrodes. The Stefan–Maxwell correlations along with the Bruggman modification illustrate the multi-species diffusion in the porous electrode. A two-equation approach is used to account for the local thermal non-equilibrium between the solid matrices and the fluids in the gas diffusion layers. In the catalyst layers, the heat generation due to overpotential heating is determined from the macroscopic electrochemical model. Computational fluid dynamics (CFD) methodology is employed to integrate electrochemical processes with co-transports of multi-physics in the PEM fuel cell. The present model is one of the first endeavors to simultaneously predict the solid-matrix temperature and the fluid-phase temperature inside a PEM fuel cell. It enables a comprehensive understanding of the mechanisms responsible for thermal pathways. Most importantly, the possibility of hot spots within a PEM fuel cell has been successfully assessed. The results obtained by the present model would be beneficial for the design of thermal management of a low-temperature fuel cell. It is also helpful in the further accurate analyses of the fuel-cell thermal performance by considering the temperature-dependent physical properties inside a fuel cell.

2. Model description

A sectional view of a typical PEM fuel cell is given in Fig. 1. The model domain is confined within a five-layer MEA (membrane-electrode assembly), i.e., two gas diffusion layers (GDLs), two catalyst layers (CLs), and a proton exchange membrane (PEM). Each GDL is in contact with an

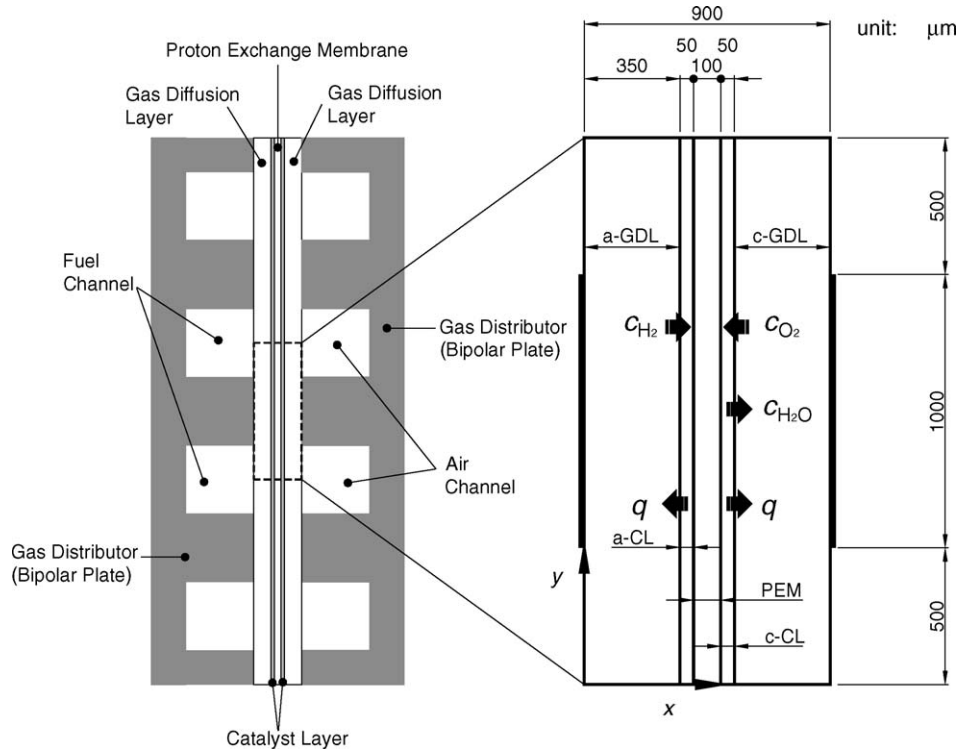

Fig. 1. Sectional view of the fuel cell module.

interdigitated gas distributor, which has an inlet channel, a current collector, and an outlet channel. Humidified hydrogen and air are supplied to the inlet channels of the anode and cathode, respectively. In the anodic catalyst layer, hydrogen is consumed to form protons that carry the ionic current to the cathode. In the cathodic catalyst layer, the electrochemical reaction not only consumes the oxygen but also produces the water. The hydrogen oxidation reaction (HOR) in the anodic catalyst layer and the oxygen reduction reaction (ORR) in the cathodic catalyst layer are, respectively, expressed as by the following equations:

$$\tfrac{1}{2}H_2 \rightarrow H^+ + e^- \quad (1)$$

$$\tfrac{1}{4}O_2 + H^+ + e^- \rightarrow \tfrac{1}{2}H_2O \quad (2)$$

Both feeds are regarded as ideal gases and are transported through diffusion and convection. The electrodes are treated as homogeneous porous media with uniform morphological properties such as porosity and permeability. All gases within each of the electrodes exist as a continuous phase. In addi-

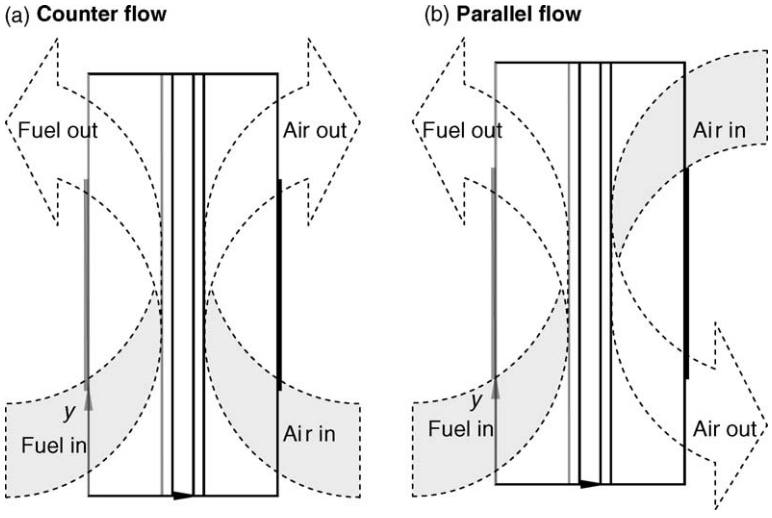

Fig. 2. Schematic drawing of the parallel-flow geometry and the counter-flow geometry.

tion, water in the vapor phase is considered to simplify the model.

In the present study, two kinds of flow orientations are examined, i.e., the counter flow and the parallel flow (Fig. 2).

2.1. Governing equations

The ionic and electronic current balances in the PEM and GDLs, based on the Ohm's law, are, respectively, described as the following equations:

$$\nabla(-\sigma_m \nabla \phi_m) = 0 \tag{3}$$

$$\nabla(-\sigma_s \nabla \phi_s) = 0 \tag{4}$$

where ϕ_m and ϕ_s are the membrane-phase potentials and the catalyst-phase potentials, respectively. σ_m and σ_s are the ionic and electronic conductivities of the PEM and GDLs, respectively.

In the catalyst layer of a PEM fuel cell, the porous matrix contains two kinds of solid phases, i.e., ionic conductor (electrolyte) and electronic conductor (catalyst). A potential difference exists between the catalyst and electrolyte to drive the transfer current (j_T), keeping the electrochemical reaction continuously. The current passes through catalyst layer can be decomposed two parts, i.e.,

$$\mathbf{i} = \mathbf{i}_s + \mathbf{i}_m \tag{5}$$

where $\mathbf{i}_s$ and $\mathbf{i}_m$ are the currents flowing through the catalyst and the electrolyte, respectively. Since the electrodes are electroneutral everywhere, there is no charge-buildup in the catalyst layers. Thus, the charge conservation is

$$\nabla \cdot \mathbf{i} = 0 \tag{6}$$

That is

$$\nabla \cdot \mathbf{i}_s = -\nabla \cdot \mathbf{i}_m \tag{7}$$

These two current components interact through electrochemical reactions. The electrons are transferred to the catalyst from the electrolyte in the anodic catalyst layer, and vice versa in the cathodic catalyst layer. Application of Ohm's law to equation yields the current conservation:

$$\nabla \cdot (-\sigma_{s,\mathrm{eff}} \nabla \phi_s) = -S_j \tag{8}$$

$$\nabla \cdot (-\sigma_{m,\mathrm{eff}} \nabla \phi_m) = S_j \tag{9}$$

where the sources terms S_j and $-S_j$ are the local transfer current densities corresponds to the HOR and ORR in the anode and cathode, respectively, creating and consuming protons.

Table 1
Porous-electrochemical properties of the present modeled fuel cell

Description		Unit	Value
Exchange current density	Anode, $\mathbf{j}_{o,a}$	$A\,m^{-3}$	5.0×10^3
	Cathode, $\mathbf{j}_{o,c}$	$A\,m^{-3}$	1.0×10^{-3}
Symmetric factor	Anode, α_a	–	1.0
	Cathode, α_c	–	0.5
Porosity	a-GDL, c-GDL, ε	–	0.5
	a-CL, c-CL, ε_c	–	0.5
Permeability	a-GDL, c-GDL, κ	m^2	1.57×10^{-12}
	a-GDL, c-GDL, κ_c	m^2	1.57×10^{-12}
Tortuosity	a-GDL, c-GDL, τ	–	1.5
	a-GDL, c-GDL, τ_c	–	1.5
Thermal conductivity	GDL, $k_{s,\mathrm{eff}}$	$W\,kg^{-1}\,K^{-1}$	1.7
	PEM, k_m	$W\,kg^{-1}\,K^{-1}$	0.5
	Anode gas, $k_{f,\mathrm{eff}}$	$W\,kg^{-1}\,K^{-1}$	0.182
	Cathode gas, $k_{f,\mathrm{eff}}$	$W\,kg^{-1}\,K^{-1}$	0.051
Electric conductivity	GDL (electronic), σ_s	$\Omega^{-1}\,m^{-1}$	300
	PEM (ionic), σ_m	$\Omega^{-1}\,m^{-1}$	14.4
Inlet pressure	Anode, $p_{in,a}$	kPa	1.013×10^5
	Cathode, $p_{in,a}$	kPa	1.013×10^5
Mass flow rate	Anode	$kg\,s^{-1}$	1.19×10^{-6}
	Cathode	$kg\,s^{-1}$	2.98×10^{-5}
Species mass fraction at cathode inlet (saturated air at STP)	Oxygen, ω_{O_2}	–	21.7%
	Water, $\omega_{H_2O,c}$	–	2.1%
	Nitrogen, ω_{N_2}	–	77.2%
	Total	–	100%
Species mass fraction at anode inlet (saturated H_2 at STP)	Hydrogen, ω_{H_2}	–	76.5%
	Water, $\omega_{H_2O,a}$	–	23.5%
	Total	–	100%

They are denoted as $\mathbf{j}_{\mathrm{T,HOR}}$ and $\mathbf{j}_{\mathrm{T,ORR}}$, respectively, in the following discussion. $\sigma_{\mathrm{s,eff}}$ and $\sigma_{\mathrm{m,eff}}$ are the effective electronic and ionic conductivities of the catalyst and electrolyte, respectively. They are modeled as

$$\sigma_{\mathrm{s,eff}} = \sigma_{\mathrm{s}}(1-\varepsilon_{\mathrm{c}}) \times \upsilon_{\mathrm{s}} \times p_{i,\mathrm{s}} \tag{10}$$

$$\sigma_{\mathrm{m,eff}} = \sigma_{\mathrm{m}}(1-\varepsilon_{\mathrm{c}}) \times \upsilon_{\mathrm{m}} \times p_{i,\mathrm{m}} \tag{11}$$

where υ_{s} and υ_{m} are the volume fraction of the catalyst and electrolyte in the catalyst layer, respectively. $p_{i,\mathrm{s}}$ and $p_{i,\mathrm{m}}$ are the possibilities of the catalyst and electrolyte in the connection of the catalyst layer, respectively [7,11]. It is noted that only a long-range connection of the same particles stretch through the entire catalyst layer ensures good conductivity.

The present model takes into account two species in the anode (H_2, H_2O), and three in the cathode (O_2, H_2O, N_2). The species transports based on the Stefan–Maxwell multicomponent diffusion are given by the following equations:

$$\rho\mathbf{u}\cdot\nabla\omega_i = \nabla\cdot\left\{\rho\omega_i\sum_{j=1}^{N}D_{i,\mathrm{eff},j}\left[\frac{M}{M_j}\left(\nabla\omega_j+\omega_j\frac{\nabla M}{M}\right)+(x_j-\omega_j)\frac{\nabla p}{p}\right]\right\}+S_i \tag{12}$$

The effective diffusivities of the species i in the porous electrode follows the Bruggman model [12], i.e.,

$$D_{i,\mathrm{eff}} = \varepsilon^{\tau}D_i \tag{13}$$

The source terms S_i represent the consumption of the reactants during the electrochemical reaction. It becomes $S_i = \mathbf{j}_{\mathrm{T,ORR}}M_{\mathrm{O_2}}/4F$ and $S_i = \mathbf{j}_{\mathrm{T,HOR}}M_{\mathrm{H_2}}/2F$ in the cathodic and anodic catalyst layers, respectively. In the gas diffusion layer it is nothing. According to the Butler–Volmer correlation [13], the relationship among the local transfer current density ($\mathbf{j}_{\mathrm{T}}$), the reactant concentrations (c_i), and phase potentials (ϕ_{s}, ϕ_{m}) can be described as the following equation:

$$\mathbf{j}_{\mathrm{T,OOR}} = \mathbf{j}_{\mathrm{o,c}}\left\{\left(\frac{c_{\mathrm{O_2}}}{c_{\mathrm{O_2,ref}}}\right)\exp\left[\frac{4\alpha_{\mathrm{c}}F}{RT}(\phi_{\mathrm{m}}-\phi_{\mathrm{s}})\right]-\left(\frac{c_{\mathrm{H_2O}}}{c_{\mathrm{H_2O,ref}}}\right)^2\exp\left[\frac{4(1-\alpha_{\mathrm{c}})F}{RT}(\phi_{\mathrm{m}}-\phi_{\mathrm{s}})\right]\right\} \tag{14}$$

$$\mathbf{j}_{\mathrm{T,HOR}} = \mathbf{j}_{\mathrm{o,a}}\left\{\left(\frac{c_{\mathrm{H_2}}}{c_{\mathrm{H_2,ref}}}\right)^2\exp\left[\frac{4\alpha_{\mathrm{a}}F}{RT}(\phi_{\mathrm{s}}-\phi_{\mathrm{m}})\right]\right\} \tag{15}$$

where $\mathbf{j}_{\mathrm{o,c}}$ and $\mathbf{j}_{\mathrm{o,a}}$ are the cathodic and anodic exchange current densities, respectively.

The fluid flow in the porous media is described by the following equations:

$$\rho\mathbf{u}\cdot\nabla\mathbf{u} = -\nabla p+\nabla\cdot(\mu\nabla\mathbf{u})+S_{\mathrm{m}} \tag{16}$$

$$\nabla(\rho\mathbf{u}) = 0 \tag{17}$$

where ρ is the density, μ the viscosity, $\mathbf{u}$ the velocity vector, and p the pressure. The source term in the momentum equations is based on the Darcy's law, representing an extra drag force proportional to fluid viscosity and velocity, and inversely proportional to the permeability of a porous medium, i.e., $S_{\mathrm{m}} = -(\mu/\kappa)\mathbf{u}$, where κ is the permeability.

As for the energy equations, the two-equation model is used to describe the thermal behaviors in the gas diffusion layer. The energy equations for fluid and solid phases, respectively, are

$$(\rho c_{\mathrm{p}})_{\mathrm{f}}\mathbf{u}\cdot\nabla T_{\mathrm{f}} = \nabla\cdot(k_{\mathrm{f,eff}}\nabla T_{\mathrm{f}})-S_{\mathrm{e,GDL}} \tag{18}$$

$$0 = \nabla\cdot(k_{\mathrm{s,eff}}\nabla T_{\mathrm{s}})+S_{\mathrm{e,GDL}} \tag{19}$$

The source terms $S_{\mathrm{e,GDL}} = -h\nu\cdot(T_{\mathrm{s}}-T_{\mathrm{f}})$ represent the thermal interaction between the solid matrices and the fluids. $h\nu$ is the interfacial heat transfer coefficient (volumetric) between the solid matrices and the reactants fluid in porous medium [14]. The effective thermal conductivities of both phases are, respectively, defined as

$$k_{\mathrm{s,eff}} = (1-\varepsilon)k_{\mathrm{s}} \tag{20}$$

$$k_{\mathrm{f,eff}} = \varepsilon k_{\mathrm{f}} \tag{21}$$

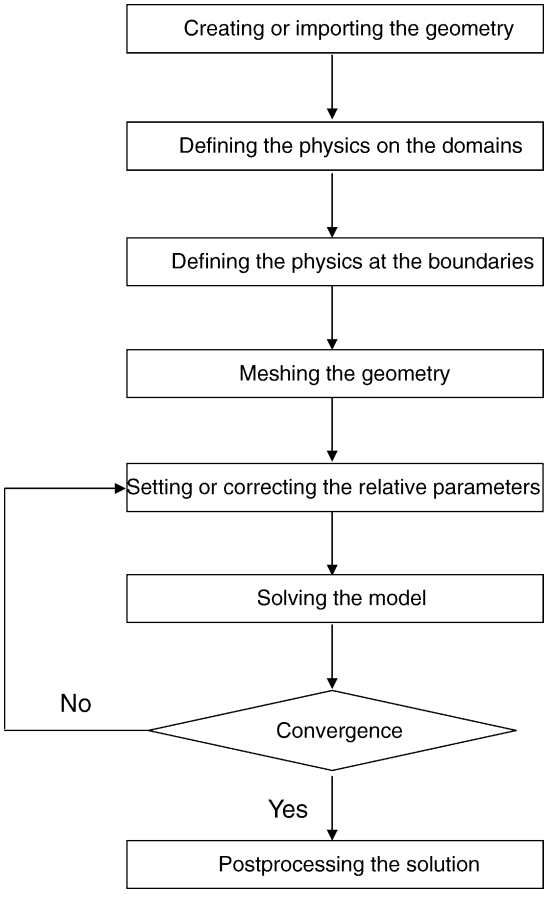

Fig. 3. Flow chart of the numerical simulation.

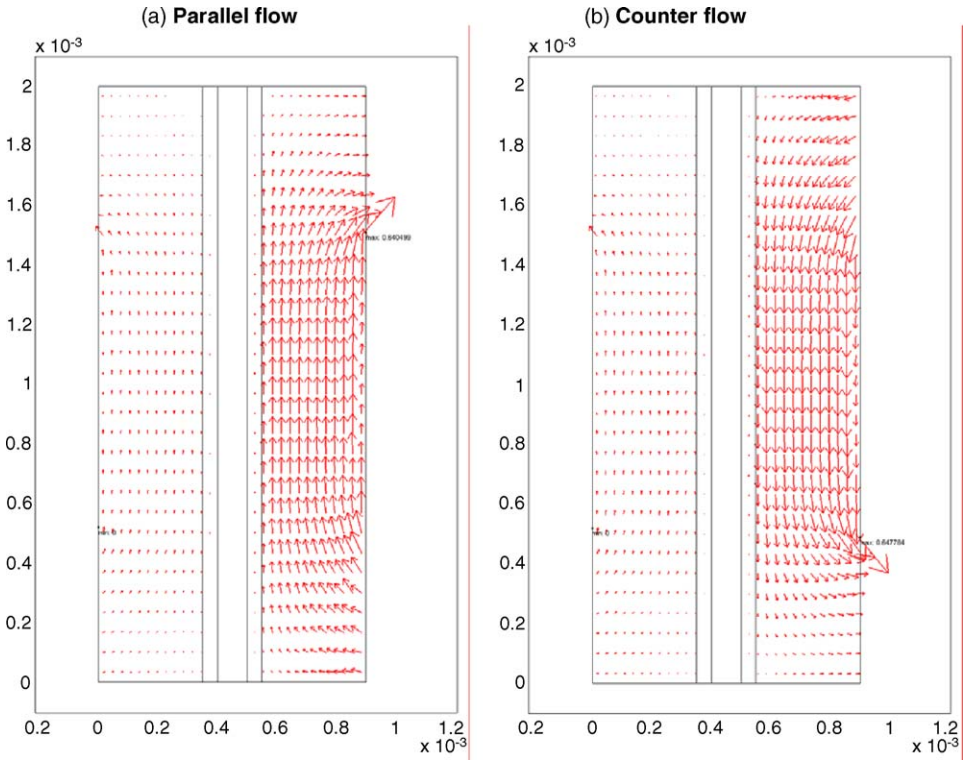

Fig. 4. Comparison of flow velocity vectors between the parallel and counter flows.

where k_s and k_f are the thermal conductivities of the solid matrix and the reactant fluid, respectively.

In the catalyst layer, the electrochemical reaction occurs at the interface of reactant fluid and catalyst. Physically, the fluid and solid phases in the catalyst layer have the same temperatures, i.e.,

$$(\rho c_p)_f \mathbf{u} \cdot \nabla T_f = \nabla \cdot (k_{c,eff} \nabla T_f) + S_{e,CL} \quad (22)$$

$$T_f = T_s \quad (23)$$

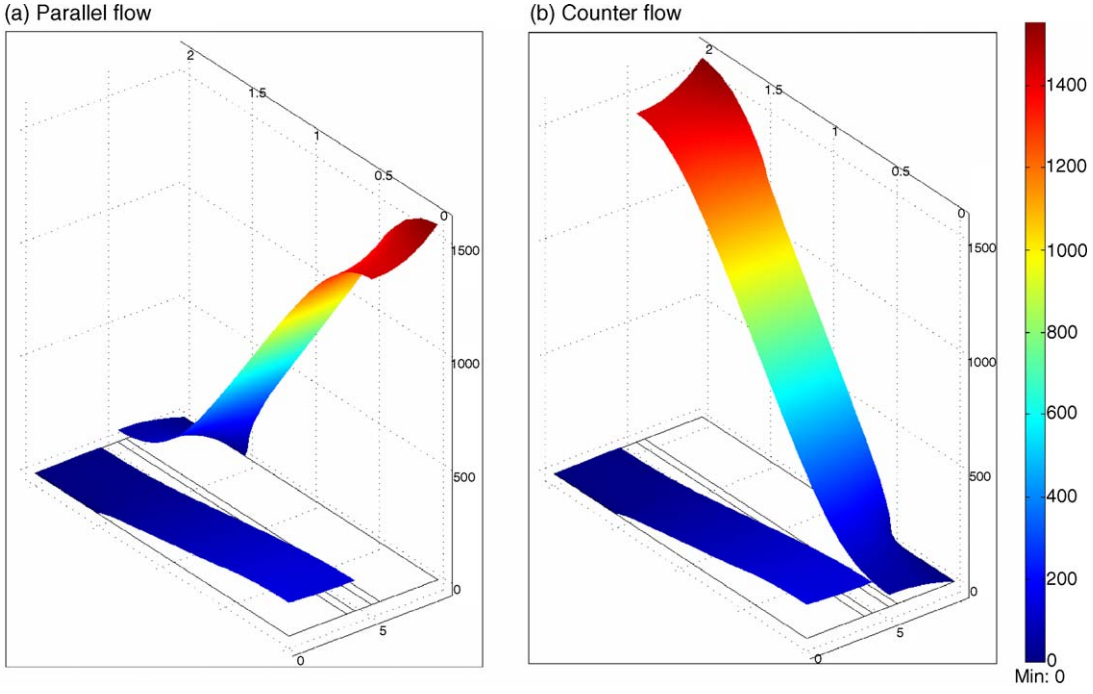

Fig. 5. Comparison of pressure distribution between the parallel and counter flows.

In the present model, the radiation heat flux and the energy dissipation due to Joule heating are neglected. Therefore, the source term in the above equation can be represented by the overpotential heating by the electrochemical activation, i.e., $S_{e,CL} = \mathbf{j}_{T,HOR} \times (\phi_m - \phi_s)$in the anodic catalyst layer and $S_{e,CL} = \mathbf{j}_{T,ORR} \times (\phi_s - \phi_m)$ in the cathodic catalyst layer, respectively. The effective thermal conductivity of the catalyst layer is determined by the following equation [12]:

$$k_{c,eff} = -2k_c + \frac{1}{\varepsilon/(2k_c + k_f) + (1-\varepsilon)/3k_c} \tag{24}$$

where k_c is the weight-averaged conductivity between the ionic conductor (such as Nafion^{TM}) and the electric conductor (such as Pt/C).

As for the PEM, a typical conduction equation is employed to describe the thermal behavior in the impermeable material, i.e.,

$$\nabla \cdot (k_m \nabla T_s) = 0 \tag{25}$$

where k_m is the ionic conductivity of the PEM.

2.2. Boundary conditions

The electrochemical and physical properties used in the calculation are given in Table 1. The temperatures for both feeds along with the surfaces of the gas distributor are fixed at 298 K. Both outlets of the module have an ambient pressure. The anode is supplied with the humidified

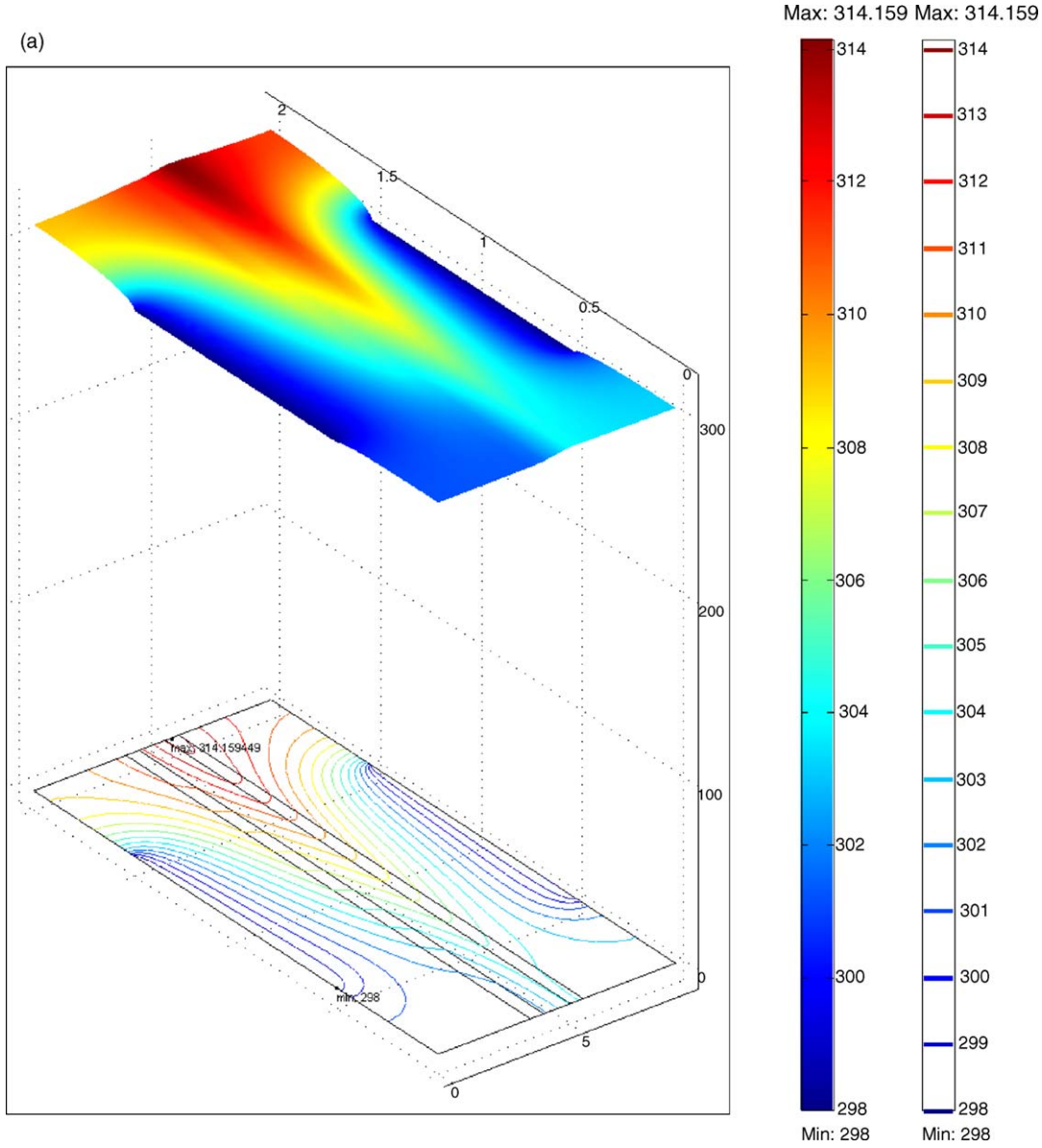

Fig. 6. Effect of total overpotential on the solid-phase temperature distributions for the parallel-flow geometry: (a) $\eta_{tot} = 0.45$ V; (b) $\eta_{tot} = 0.65$ V.

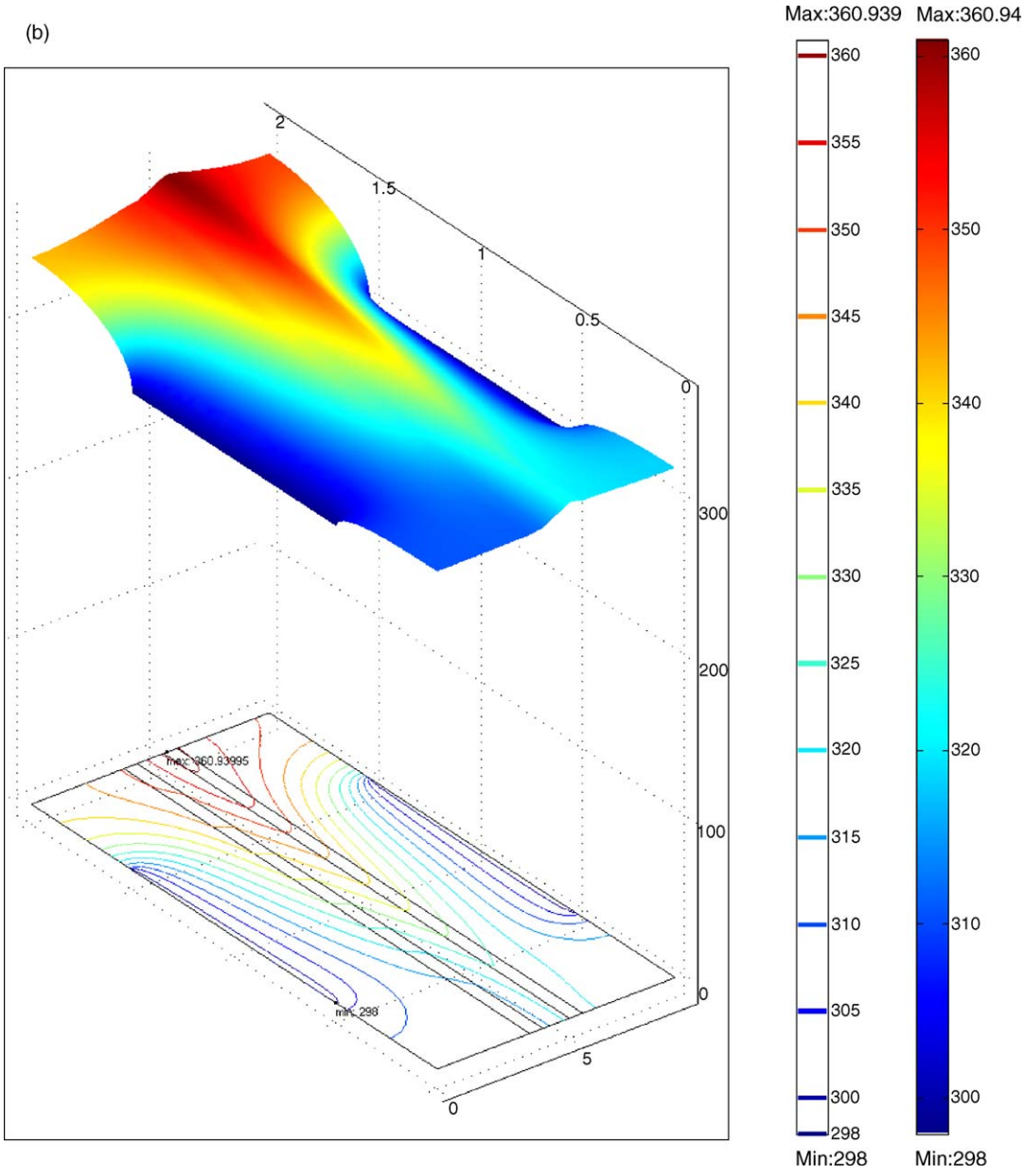

Fig. 6. (*Continued*).

hydrogen of mass fractions of 76.5/23.5% for H_2/H_2O. The cathodic side feeds with the saturated air of 21.7/2.1/77.2% for $O_2/H_2O/N_2$, where N_2 is considered as an inert gas and serves as diluents. Reactants delivered to the cathode and anode are 2.98×10^{-5} and 1.19×10^{-6} kg s^{-1}, respectively. The difference of electronic-conductor potential (ϕ_s) between two contact surfaces between the electrodes and gas distributors represents the total overpotential (η_{tot}) across the five-layer MEA. The potential at the contact surfaces between the c-GDL and the current collector is arbitrarily chosen to be zero, while the total overpotential is used as boundary condition at the anodic current collector. For the rest of the boundaries they have either insulation or symmetry conditions.

2.3. Numerical methods

The solutions of the above equations are obtained with a general purpose commercial solver, Femlab. It uses the Broyden's method with an LU-decomposition pre-conditioner to solve the non-linear equations iteratively. To reduce continuity errors, a penalty term is employed for pressure. Thus, there is a continuous part of the pressure and piecewise constant part providing and extra DOF (degree of freedom) for pressure on each element. It uses Newton–Raphson iteration to solve the close-coupled groups (velocity, pressure, temperature, concentration and electricity) and uses the frontal algorithm (Gaussian elimination) to solve the linearized system of equations for each iteration. In the computational domain,

a total of 1828 nodes and 8789 elements were used (quadratic velocities in each direction), with a fine mesh throughout the region. The program gives results within 1% of each other on the finest meshes used. The iterations proceeded until the change in the calculated air flow rate between 20 consecutive iterations was less than 0.1%. In order to achieve that, the necessary number of iterations varied between 200 and 350. The CPU time ranged from 10 to 100 min on a Pentium IV PC (2.8 GHz, 2 GB RAM) using Windows XP operating system. Fig. 3 shows a flow chart of the present numerical modeling.

3. Results and discussion

Fig. 4 compares the flow velocity distributions between the parallel-flow geometry and the counter-flow geometry. The point marks on each plot mean the local maximum and minimum velocities in the module. It is seen that the fuel side (anode) has a lower velocity than the air side (cathode) since it has a smaller stoichiometric coefficient. Results also show that the maximum velocity occurs at the cathode exit around the rib surface. The flow around the corners formed by the symmetric planes ($y = 0$, and 2.0 mm) and the interfaces

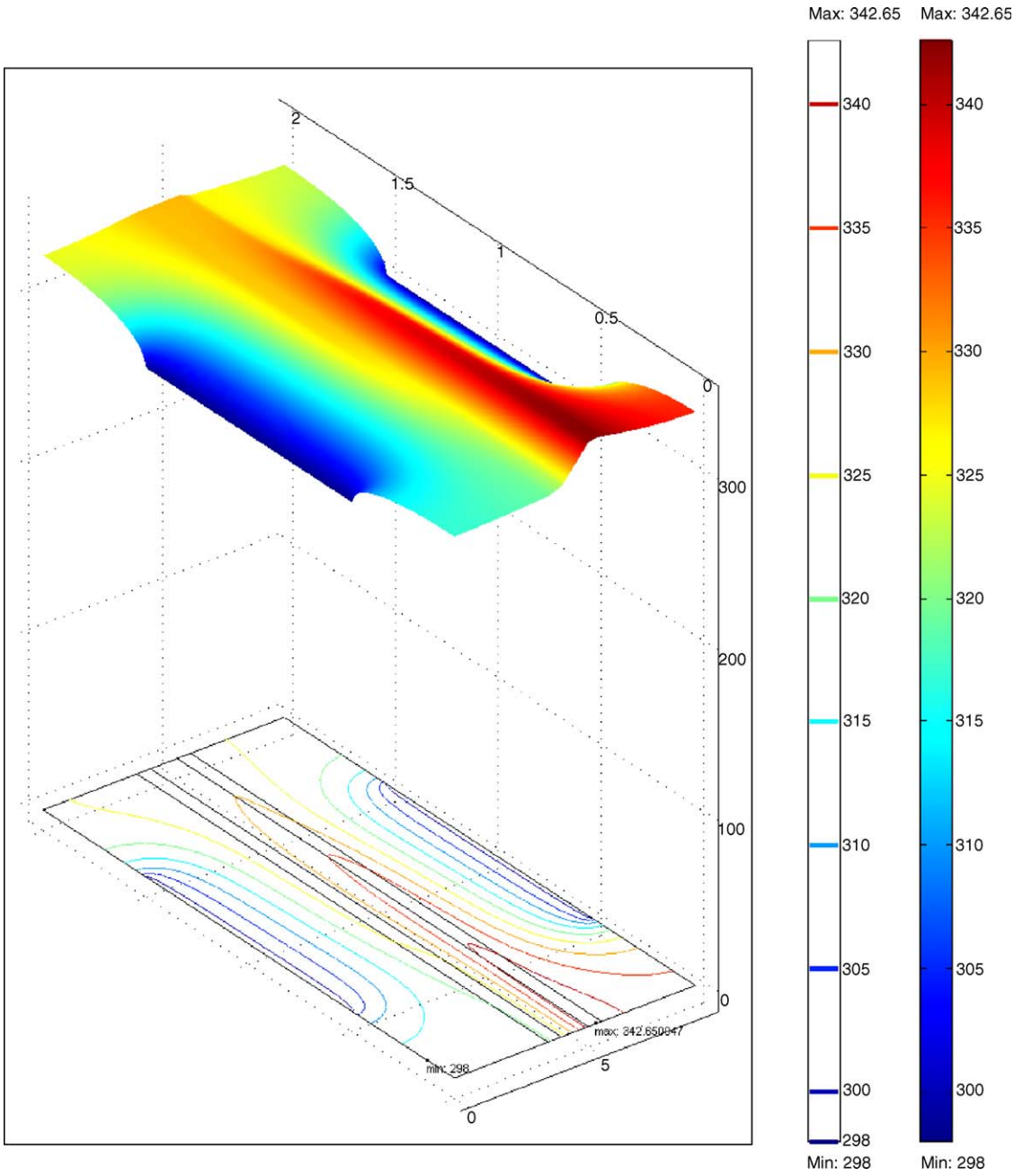

Fig. 7. Solid-phase temperature distributions of the counter-flow geometry for $\eta_{tot} = 0.65$ V.

between the PEM and catalyst layers ($x = 0.4$ and 0.5 mm) is nearly stagnant. Fig. 5 shows a comparison of the pressure distribution in the parallel-flow geometry and counter-flow geometry. Both outlets of the module are opened to the ambient, which serve as reference pressures. It is seen that the pressure drops across the cathode is significantly higher than that across the anode, typically about 1.5 and 0.15 kPa for the cathode and the anode, respectively. This is because a higher fluid density is accompanied by the cathode flow, and a more fluid should be driven across the cathode (Table 1). In general, the pressure drop characteristics are not affected by the flow direction in essential.

3D mappings of the solid-phase temperatures for the parallel-flow geometry and the counter-flow geometry are shown in Figs. 6 and 7, respectively. The corresponding projects showing the isothermal contours are also provided in these figures. The point marks shown on each plot indicate the maximum or minimum temperatures in the module.

Fig. 6(a) and (b) shows the effect of total overpotential (η_{tot}) on the solid-phase temperature distributions for the

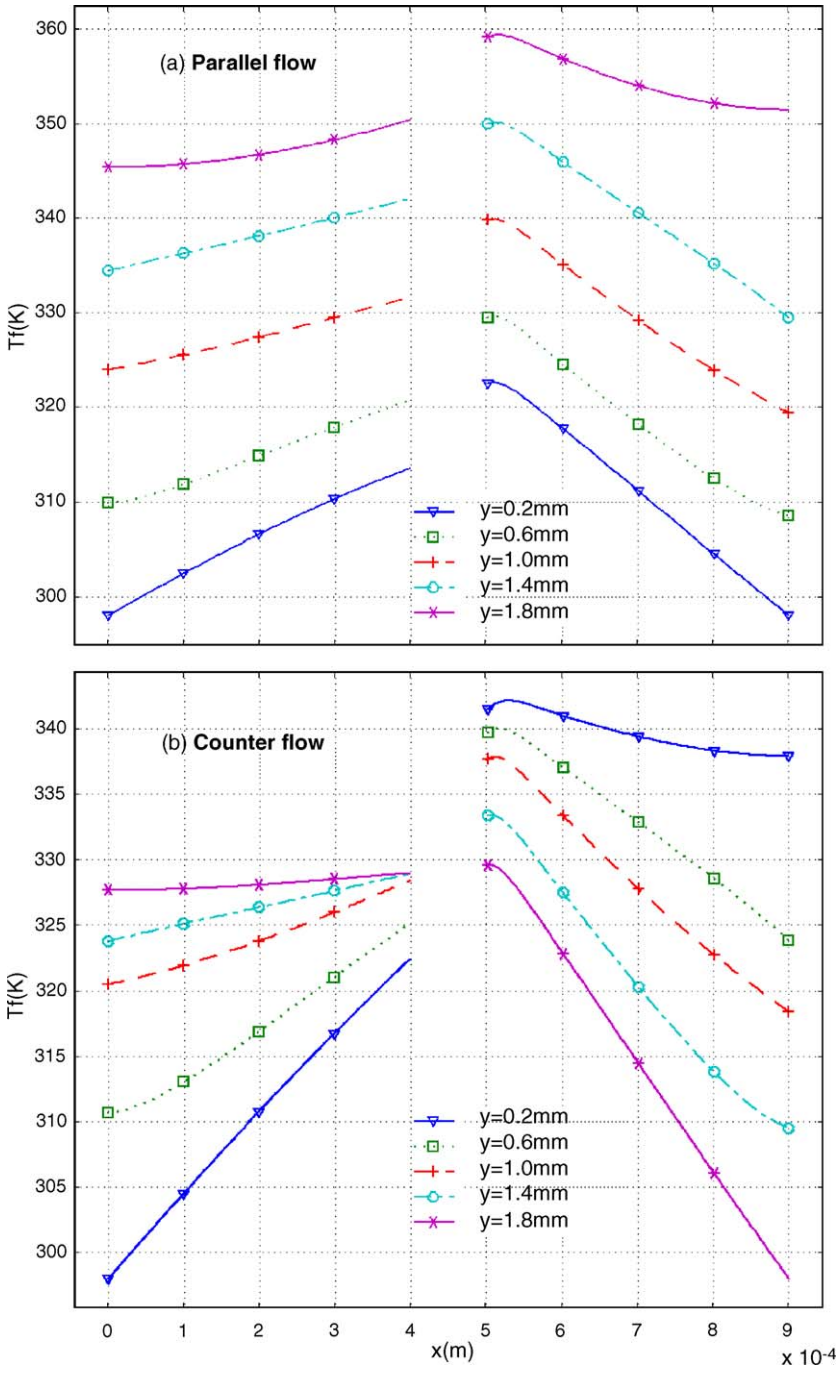

Fig. 8. Comparison of fluid-phase temperature distributions at several y stations between parallel flows and counter flows, $\eta_{tot} = 0.65$ V.

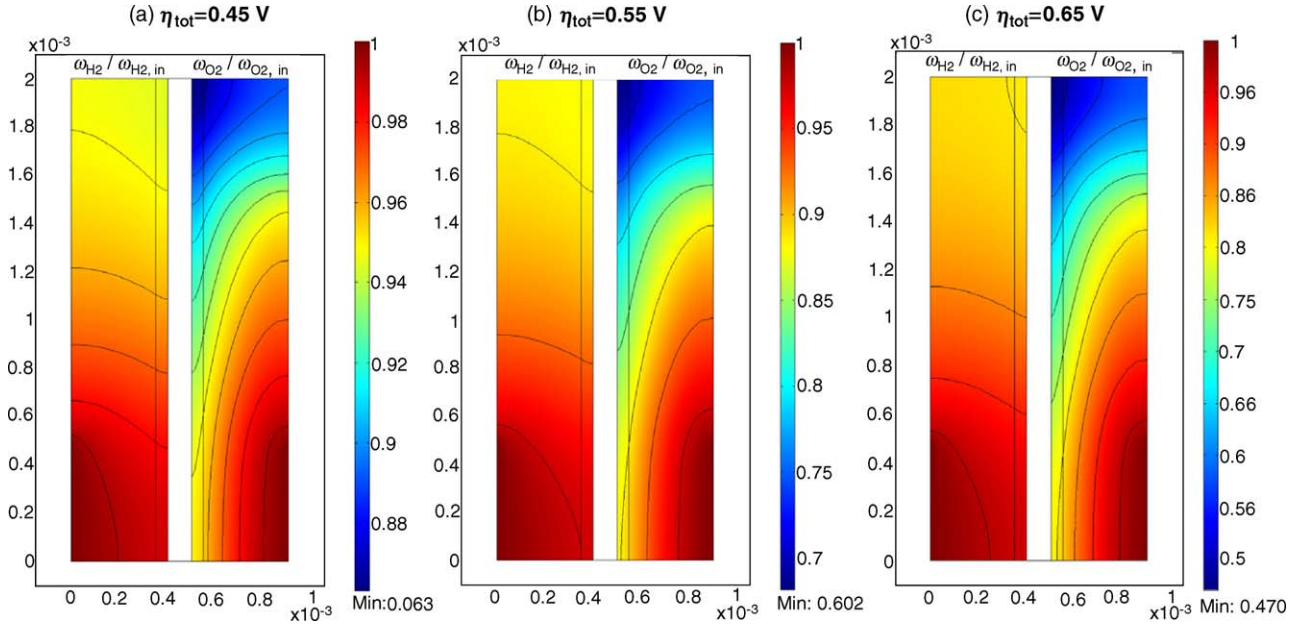

Fig. 9. Effect of total overpotential on the concentration distribution in the computational module.

parallel-flow geometry. It is seen that the solid-phase temperature in the cathode is higher than that in the anode. This is because the c-CL dissipates more heat by the electrochemical reaction than the a-CL. The maximum temperature occurs in the c-CL cutting across the upper symmetric plane ($y = 2.0$ mm). In addition, the region near the rib surface has a low solid phase temperature. Near the fuel and oxidant entrances, the solid phase has low temperatures due to the significant forced convection by the inlet fluid. When the total overpotential increases form $\eta_{tot} = 0.45$–0.65 V, as shown in Fig. 6(b), the solid-phase temperature distribution becomes more uneven. In addition, the maximum solid-phase temperature increases from 314 to 361 K.

Fig. 7 shows the results of the counter-flow geometry with the same total overpotential as that in Fig. 6(b). Again, the minimum solid-phase temperatures occur in the region near the rib surfaces ($y = 0$ and 0.9 mm). However, the maximum solid-phase temperature has moved to the bottom of the module, i.e., at the c-CL cutting across the middle of cathode exit ($y = 0$). The peak of the solid-phase temperature is reduced from 361 to 343 K with the parallel-flow geometry instead of the counter-flow geometry. This is because the heat dissipated by the overpotential heating near the cathode outlet is somewhat cooled down by the anode inlet flow that removes the conduction heat through the PEM.

Fig. 8(a) and (b) shows the fluid-phase temperature distribution along several elevations (i.e., $y = 0.2$, 0.6, 1.0, 1.4, 1.8 mm) cutting across the module for the parallel-flow geometry and the counter-flow geometry, respectively. Since the PEM is impermeable, no data are shown in the region of $0.4\text{ mm} < x < 0.5$ mm. In both flow geometries, the fluid-phase temperature in the cathode is higher than that in the anode. This is because the significant heat generation in the cathodic catalyst layer. A stronger electrochemical kinetics of HOR (i.e., higher exchange current density, Table 1) in the a-CL requires a less overpotential to drive the through-flow current in the fuel cell. Consequently, a less overpotential heating in the a-CL results in a lower temperature. The fluid-phase temperature increases downstream due to the heat accumulation for both electrodes. The maximum fluid-phase temperature for the parallel-flow geometry is higher than the counter-flow geometry.

Fig. 9 shows the effect of total overpotential on the concentration distribution in the module for the parallel-flow geometry. The data shown in the plots are normalized by

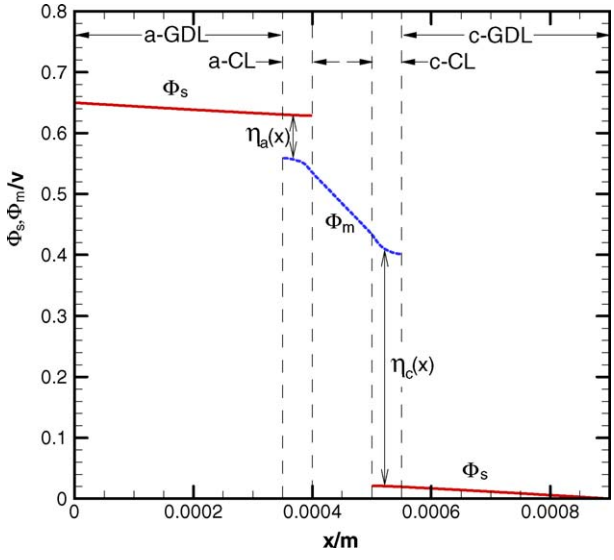

Fig. 10. Voltage of the catalyst phase and membrane phase along the mid-plane of the module.

the corresponding inlet concentration, i.e., $\omega_{H_2}/\omega_{H_2,in}$ for the anode and $\omega_{O_2}/\omega_{O_2,in}$ for the cathode. It is seen from these figures that an increase of total overpotential increases the fuel and oxidant utilization in both electrodes. At a fixed total overpotential, the local concentration decreases along the flow direction. Also, it decreases as the flow approaches the catalyst layer. It is further seen that the concentration gradient along the x direction in the cathode is more significant than that in the anode. This is because cathode has a higher velocity (Fig. 4) that dominates the species transport via forced convection. In contrast, the flow velocity in the anode side is relatively stagnant (Fig. 4). The diffusion becomes more significant in the species transports.

Fig. 10 shows the distribution of the phase potential at the elevation cutting across the module mid-plane ($y = 1.0$ mm). The solid lines are the catalyst-phase potential while the dashed line is the membrane-phase potential. The differences between the above potentials in the catalyst layers represent the activation overpotentials, i.e., $\eta_a = \phi_c - \phi_m$ in the a-CL and $\eta_c = \phi_m - \phi_c$ in the c-CL. The activation overpotentials in both catalyst layers increases along the depth of the catalyst layer. That is the largest activation overpotentials occur at the both sides of the PEM. The activation overpotential drop in the c-CL is significantly higher than that in the a-CL. In the GDLs and PEM, a linear drop of phase potential is found. The slope in the PEM is higher than that in the GDLs meaning that the Ohmic loss in the PEM is higher that in the GDLs.

Fig. 11(a) shows a full-field distribution of the local current density in the module. It is seen that the current directs form the surfaces in contact with the anodic gas distributors toward the surfaces in contact with the cathodic gas distributors. The current density is high near the rib surface corner and is low near the module corner. Fig. 11(b) is a local magnification showing the current density distribution in the catalyst layers near the module middle. As shown in Fig. 11(b), the current density in the a-CL gradually decreases along the current direction, i.e., from the interface of the GDL and the catalyst layer (i.e., $x = 0.35$ mm) to the PEM. This is because

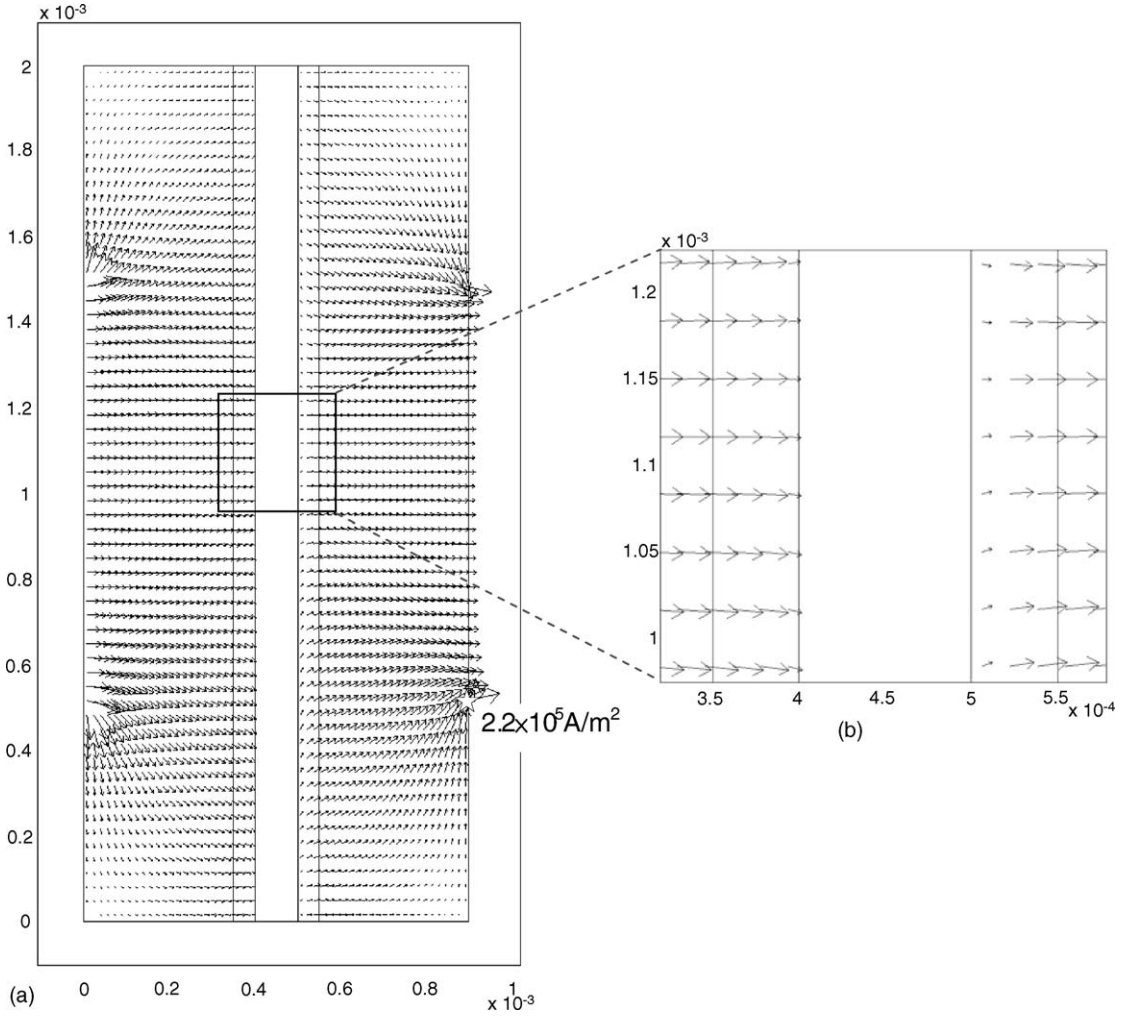

Fig. 11. Distributions of current density vectors: (a) the entire computational module; (b) magnification around the catalyst layers.

of the HOR consumes the current. In contrast, the current density is gradually recovered in the c-CL from the interface of the PEM and the c-CL ($x = 0.50$ mm) to the c-GDL due to the ORR.

4. Concluding remarks

A multi-physics model has been developed to investigate the thermal-electrochemical transports in a PEM fuel cell. Conservative equations governing the co-transports of mass/momentum/heat/species/charge are numerically solved with proper account of electrochemical kinetics. In the catalyst layer, a general energy equation is derived using the volume-averaging technique, along with a local heat generation resulting from electrochemical reactions. In the gas diffusion layer, a two-equation thermal transport model is developed to resolve the fluid and solid phase temperatures for the first time. Results show that both the solid-matrix temperature and the fluid-phase temperature increase with increasing the total overpotential (η_{tot}). Under the same total overpotential, the maximum solid-phase temperature is reduced by replacing the parallel-flow geometry with the counter-flow geometry.

The present paper has provided an innovative aspect in the heat transfer of fuel-cell related studies. It has successfully predicted the fluid and solid phase temperatures inside a fuel cell simultaneously for the first time. It is important to understand the electrochemical/thermal coupled mechanisms responsible for thermal pathways in a low-temperature fuel cell. The thermal effect on the active material degradation and hence fuel cell durability will be studied in the future work.

Acknowledgment

This research was partly sponsored by the National Science Council of Taiwan under contract no. NSC 92-2212-E-451-002.

References

[1] D.M. Bernardi, M.W. Verbrugge, AIChE J. 37 (1991) 1151.
[2] D.M. Bernardi, M.W. Verbrugge, J. Electrochem. Soc. 139 (1992) 2477.
[3] T.E. Springer, T.A. Zawodinski, S. Gottesfeld, J. Electrochem. Soc. 136 (1991) 2334.
[4] T.E. Springer, M.S. Wilson, S. Gottesfeld, J. Electrochem. Soc. 140 (1993) 3513.
[5] T.V. Nguyen, R.E. White, J. Electrochem. Soc. 140 (8) (1993) 2178–2186.
[6] T.F. Fuller, J. Newman, J. Electrochem. Soc. 140 (5) (1993) 1218–1225.
[7] V. Gurau, H. Liu, S. Kakac, AIChE J. 44 (11) (1998) 2410–2421.
[8] S. Shimpalee, S. Dutta, Effect of Humidity on PEM Fuel Cell Performance. Part II: Numerical Simulation, HTD-vol. 364-1, Heat Transfer Division, ASME, 1999.
[9] T. Zhou, H. Liu, A general three-dimensional model for proton exchange membrane fuel cells, Part I, J. Trans. Phenom. 3 (3) (2001) 177–198.
[10] S. Um, C.Y. Wang, Computational fluid dynamics modeling of proton exchange membrane fuel cells, J. Electrochem. Soc. 147 (12) (2000) 4485–4493.
[11] J.J. Hwang, C.K. Chen, R.F. Savinell, C.C. Liu, J.C. Wainright, J. Appl. Electrochem. 34 (2004) 217.
[12] J. Bear, J.M. Buchlin, Modeling and Application of Transport Phenomena in Porous Media, Kluwer Academic Publishers, Boston, MA, 1991.
[13] P. Costamagna, K. Honegger, J. Electrochem. Soc. 145 (1998) 3995.
[14] J.J. Hwang, G.J. Hwang, R.H. Yeh, C.H. Chao, J. Heat Transf. 124 (2002) 120.